

Progress on Optical Verification for Occulter-Based High Contrast Imaging

Dan Sirbu ¹, N. Jeremy Kasdin ¹, Robert J. Vanderbei ²

¹ Department of Mechanical and Aerospace Engineering, Princeton University

² Department of Operations Research and Financial Engineering, Princeton University

ABSTRACT

An external occulter is a specially-shaped spacecraft flown in formation with a telescope. It enables high-contrast imaging of the dim planetary companions of the neighboring solar system by blocking starlight before it reaches the entrance pupil. Occulters have to be designed via optimization methods that account for diffraction to most effectively block starlight. To predict occulter performance, we must verify the fidelity of the optical propagation models under scaled conditions. In this paper, we measure the contrast of a scaled occulter. The validity of the contrast calibration is determined using a baseline circular occulter. We verify contrast better than 10^{-10} , however the measurements do not perform as well as the prediction from theoretical modelling. We attribute this difference to glint scattering off mask edges.

Keywords: External Occulters, High Contrast Imaging, Optimization, Scalar Diffraction, Optical Verification

1. INTRODUCTION

Direct imaging of an Earth-like planet around nearby stars represents a challenge for two primary reasons. First, the intensity ratio between the bright star and its dim Earth-like planetary companion is expected to be approximately ten orders of magnitude.¹ Secondly, the habitable zone of an Earth-like planet is at a small angular separation to the star – for a Sun-like star that is 30 light years away the angular separation of the inner portion of the habitable zone could fall about within 75 milliarcseconds. Normally, the wings of the point spread function (PSF) of the star obscure the much dimmer PSF of the planet and a number of mission concepts have been proposed to work around this problem.

An external occulter is such a mission concept that deals with the star's PSF by blocking most of the starlight before it reaches the telescope pupil as shown in Figure 1. It thus enables high-contrast imaging of the dim planetary companion outside of the occulter's geometric inner working angle. It has been known for a long time that a simple circular disk will not be sufficient to create the high-suppression shadow required for imaging planets; because of diffraction there is insufficient suppression in the shadow.² Instead, the edge of the occulter has to be specially-shaped so that the shadow darkness is minimized over a region that will cover the entire extent

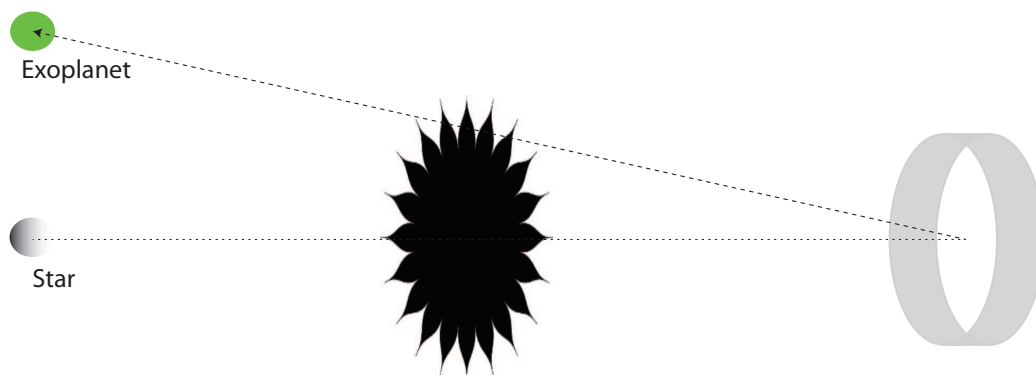


Figure 1: Schematic of occulter mission concept. The occulter blocks starlight from reaching the telescope pupil, but allows light from the exoplanet.

of the telescope. This can be formulated as an optimization problem with the size of the occulter, extent of the desired shadow, observation wavelengths, angular size, and various manufacturing limitations incorporated as constraints of a suppression maximizing objective function. In general, proposed occulters range from flagship-class such as THEIA³ and the New Worlds Observer⁴ to probe-class such as O₃⁵ and NWP.⁶ These designs feature occulters tens of meters in diameter and separated from the telescope by tens of thousands of kilometres.

Optical verification of the performance of occulter designs is nearly impossible due to the long baselines involved in space. When directly scaled to laboratory size, features of the occulter mask become subwavelength violating assumptions of the diffraction propagations used to design the occulters. Therefore, in order to test occulters our approach is to verify the fidelity of the diffraction models for purposely-designed laboratory masks. This gives us confidence to use the same optical models to predict the performance of space-sized occulter designs.⁷

In this paper we measure the contrast performance of a laboratory occulter and compare this to theoretical predictions. To verify the validity of the contrast calibrations, we use a baseline circular occulter. The paper is organized as follows. In Section 2 we describe the experimental design, including the scaling used to fit the occulter to laboratory size. In Section 3, we present our experimental measurements of occulter contrast for both the optimized and for the circular occulter. In Section 4, we present our optical equations used to predict the theoretical performance of the occulter and present our simulation results. In Section 5, we discuss the differences between the theoretical and experimental results, and postulate that the contrast is limited by glint scattered from the edges of the occulter mask.

2. EXPERIMENTAL DESIGN

An external occulter is an opaque screen designed to minimize the effects of diffraction so that the shadow cast on the pupil of a telescope downstream of the occulter is optimally dark. In this section, we discuss how space occulters can be scaled to laboratory size while maintaining the validity of the optical model, and describe details of the experimental design.

2.1 Laboratory Scaling

We are interested in the electric field $E_{\text{ap}}(\rho)$ of wavelength λ at a distance z downstream from the occulter. This is given by the Fresnel propagation for an incident beam with electric field $E_{\text{in}}(r)$ on a smooth, circularly-symmetric, apodized hole having a transmittance profile $A(r)$ with range $[0, 1]$, where r is the radial distance along the occulter plane and ρ is the radial distance along the pupil plane:⁸

$$E_{\text{ap}}(\rho) = \frac{2\pi}{i\lambda z} e^{\frac{\pi i}{\lambda z} \rho^2} \int_0^R E_{\text{in}}(r) e^{\frac{\pi i}{\lambda z} r^2} J_0\left(\frac{2\pi r \rho}{\lambda z}\right) A(r) r dr \quad (1)$$

R is the maximum radial extent of the partially-transmissive hole. The incident electric field at the occulter plane is E_{in} , and J_0 is the zeroth order Bessel function of the first kind arising due to the circular geometry.

Next, we wish to scale the occulter from space-size to lab-size. This scaling is primarily driven by the propagation distance available in our laboratory space. Therefore, we introduce the scaling factor s keeping the Fresnel numbers $\frac{r^2}{\lambda z}$ and $\frac{\rho^2}{\lambda z}$ constant. Using wavelength to scale is another possibility, but we choose to remain in the optical regime for ease of laboratory experimentation and also because occulter-assisted science will be in the optical wavelengths. The scaled distances are linear in the two transverse directions ($r' = r/s$, $\rho' = \rho/s$) and quadratic along the separation ($z' = z/s^2$), which is important because this allows us to scale to lab size. The electric field downstream from the occulter can then be re-written under the scaled dimensions:

$$E'_{\text{ap}}(\rho') = \frac{2\pi}{i\lambda z'} e^{\frac{\pi i}{\lambda z'} \rho'^2} \int_0^{R'} E'_{\text{in}}(r') e^{\frac{\pi i}{\lambda z'} r'^2} J_0\left(\frac{2\pi r' \rho'}{\lambda z'}\right) A'(r') r' dr' \quad (2)$$

where in the above, we made the following substitutions $R' = R/s$, $E'_{\text{out}}(\rho') = E_{\text{out}}(s\rho')$, $A'(r') = A(sr')$, and $E'_{\text{in}}(r') = E_{\text{in}}(sr')$.

The key point in this discussion is that Equation 1, which represents the optical propagation for an apodized occulter hole in space, is unchanged to Equation 2 for scaled laboratory dimensions except for leading phase terms. One important limitation of this approach should be noted, namely that, while this scaling maintains constant Fresnel numbers and an unchanged diffraction integral, it does, however, mean that the geometric ratios change. Therefore, the inner working angle defined by the occulter edge is increased in the lab compared to what we would expect in space.

We use an expanding beam to circumvent the problem of phase aberrations due to collimating optics, and we introduce a scaling that maintains the functional relationship for the diffraction integral in the presence of the expanding beam. An added benefit of this approach is that it expands the size of the dark hole allowing us to further reduce the separation distances to a reasonable laboratory scale. We consider a scaling factor γ which is applied to the two transverse planes in the following manner. The radial distance across the occulter plane is scaled as $r'' = r'/\gamma$, whereas the radial distance across the telescope pupil plane is scaled as $\rho'' = \gamma\rho'$. The separation distance remains unchanged ($z'' = z'$). Applying the spherical input beam, and by choice of the scale factor $\gamma = \sqrt{1 + \frac{z'}{h}}$ we obtain:

$$E''_{\text{ap}}(\rho'') = \frac{2\pi}{i\lambda z'} \frac{E_0 \gamma^2}{h} e^{\frac{2\pi i}{\lambda} h} e^{\frac{\pi i}{\lambda z'} \frac{\rho''^2}{\gamma^2}} \int_0^{R''} e^{\frac{\pi i}{\lambda z'} r''^2} A''(r'') J_0\left(\frac{2\pi r'' \rho''}{\lambda z'}\right) r'' dr'' \quad (3)$$

Thus, again this diffraction integral is unchanged compared to the space case except for a leading constant phase term and a constant multiplication factor.

2.2 Mask Design

We first design an occulter for space dimensions which we shrink to laboratory size. Additionally, we design an outer ring that minimizes the effect of diffraction in the central part of the shadow; thus we have an annular transmissive region. The outer ring allows us to use support struts to the inner occulter. The smooth optimized apodization profile can be petalized to a binary occulter mask as shown in Figure 2, with the support struts appearing by multiplication with a scale factor $b = 0.9$.

For the design of the inner occulter mask, as proposed in,⁹ we formulate an optimization problem that minimizes an objective function defined as the contrast. The radial apodization profile of the occulter is the complement of the apodized hole $A(r)$, which is discretized at midpoints. We pose constraints independently on the real and imaginary parts of the electric field at the pupil plane of the shadow.

$$\begin{aligned} \min : & \quad c & (4) \\ \text{subj. to :} & \quad -\frac{c}{\sqrt{2}} \leq \text{Re}(E_{\text{occ}}(\rho; \lambda)) \leq \frac{c}{\sqrt{2}} \\ & \quad -\frac{c}{\sqrt{2}} \leq \text{Im}(E_{\text{occ}}(\rho; \lambda)) \leq \frac{c}{\sqrt{2}} \\ & \quad c \geq 0 \\ & \quad A(r) = 1, 0 \leq r \leq a \\ & \quad A'(r) \leq 0, |A''(r)| \leq \sigma, \forall 0 \leq r \leq R \end{aligned}$$

Additional constraints are in the form of smoothness and monotonicity conditions on the apodization profile, and a central opaque disk; σ represents the smoothness condition threshold, a the extent of the opaque central disk, c is the contrast, and $[\lambda_{\min}, \lambda_{\max}]$ defines the shadow passband. To design the outer ring we reformulate the optimization problem by minimizing the difference between the electric field due to the occulter only and the complete annular apodization profile.

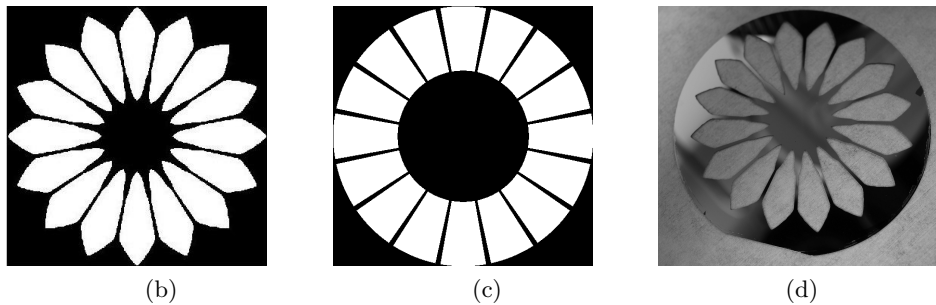
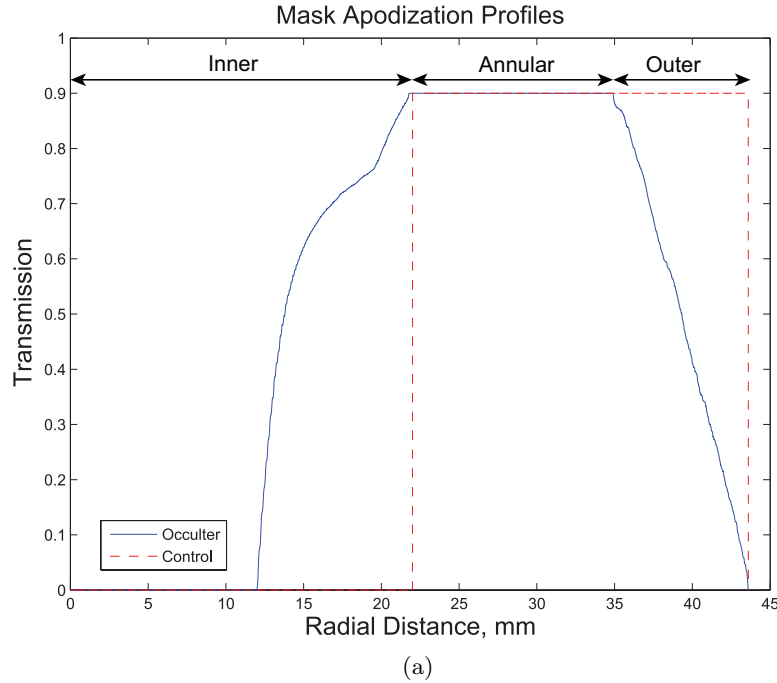


Figure 2: (a) A comparison of the apodization profiles for the optimized occluder mask and for the control mask. (b) Sixteen petal binary realization of occluder mask (c) Circular occluder baseline mask with sixteen support strut. (d) Picture of the silicon-etched occluder mask used in the laboratory.

The binary mask is created from $N = 16$ petals that are defined by turning the apodization profile into the edge of the binary mask,¹⁰ with opaque points on the mask belonging to the set S :

$$S = \{(r, \theta), 0 \leq r \leq R, \theta \in \Theta(r)\} \quad (5)$$

$$\Theta(r) = \bigcup_{n=0}^{N-1} \left[\frac{2\pi n}{N} - \frac{\pi}{N} A(r), \frac{2\pi n}{N} + \frac{\pi}{N} A(r) \right] \quad (6)$$

The occluder mask was fabricated at the Microdevices Lab at JPL using Deep Reactive Ion Etching (DRIE) to etch the open areas of the occluder mask¹¹ with micron level feature accuracy at the edges. The silicon wafer is 101.6 mm in diameter and 400 μm in thickness. The DRIE process results in vertical etches of the sidewall and thus steps were used to thin the sidewall to 50 μm . A 100 nm titanium coating was applied to increase the optical absorption to several orders of magnitude beyond the expected level of light in the shadow of the mask.

2.2.1 Control Mask

We designed a simple mask that consists of a circular occluder with supporting struts to a circular outer edge to act as a baseline for the performance of the optimized mask. The transmission profile corresponding to the

Parameter	Laboratory	Space Equivalent
Pinhole-to-occulter distance	1.5 m	Infinity
Occulter-to-camera distance	9.1 m	97,000 km
Radius of dark zone	13 mm	12 m
Occulter diameter	45 mm	380 m
Outer occulter diameter	89 mm	N/A
Inner Working Angle	8.4 arcmin	400 mas
Outer Working Angle	17 arcmin	N/A
Telescope diameter	14 mm	17 m

Table 1: Summary of experimental parameters and their equivalent space scaling.

control mask consists of a fully transmissive region starting at a radius that corresponds to the outer tip of the inner petals of the high-contrast mask and extending to a radius that corresponds to the outermost open part of the high-contrast mask. This transmission profile is then multiplied by the same scaling factor $b = 0.9$ as for the occulter mask to create support struts. The resulting apodization profile is shown in Figure 2(a). An identical petalization process as described in Equations 5 and 6 for the occulter mask is applied to obtain a binary realization of the control mask resulting in 16 support struts between the inner circular disk and the outer circular edge. The control mask was manufactured out of copper via etching, which has less accurate edge features than the DRIE method; however, the expected level of light in the shadow is greater hence significantly relaxing the tolerance on the edge features.

2.3 Experimental Setup

The occulter testbed consists of a large enclosure $40' \times 4' \times 8'$ that blocks ambient light. There are two passively isolated Newport optical tables at each end of the enclosure. The larger optical table contains the optics that create an artificial star, which consists of a diverging beam. The smaller optical table at the opposite end of the enclosure contains the telescope optics for observation of the artificial star and consists of a camera mounted on two long-travel stages that provide two degrees of freedom of movement in the lateral and vertical directions. The layout is shown schematically in Figure 3.

The light source is a single-mode 2mW HeNe laser operating monochromatically at 632 nm. To create the diverging beam the laser beam is focused onto a 15 μm pinhole. We use a diverging beam through a pinhole so that the pinhole acts as a spatial filter that removes high-frequency aberrations due to surface error on the optics. The diverging beam propagates 1.5 m before encountering the occulter mask which it overfills at the end of the optical table. Baffles are placed around the occulter mask extending to the walls of the enclosure and a further two sets of full wall baffles are located downstream to ensure no light propagates to the camera around the annular mask and to minimize any scattered light. The mask is tilted 5° to eliminate a ghost reflection by directing the back-reflection into a black-foil beamdump.

Beyond the occulter mask, the beam propagates 9.1 m to the second optical table on which a camera is placed on two 300 mm long-travel stages; both move perpendicular to the propagation direction, one horizontally and one vertically. Together these stages allow the camera to be precisely aligned in the shadow cast by the occulter. The camera is an astronomical-grade thermoelectrically cooled Starlight Xpress SXV-H9 CCD. A telephoto lens set at $f = 300$ mm is outfitted via the M42 mount, and the smallest available aperture setting at $f/22$ is used to form an iris – at 14 mm this is smaller than the designed dark hole (see Table 1). The CCD has pixel pitch of $6.45 \mu\text{m} \times 6.45 \mu\text{m}$.

Contrast is measured with the camera lens with the focus set on the pinhole source. The contrast is the ratio between the intensity of each pixel in the image formed when the mask is in place and the intensity of the peak pixel of the point spread function without a mask, calibrating for different exposures.

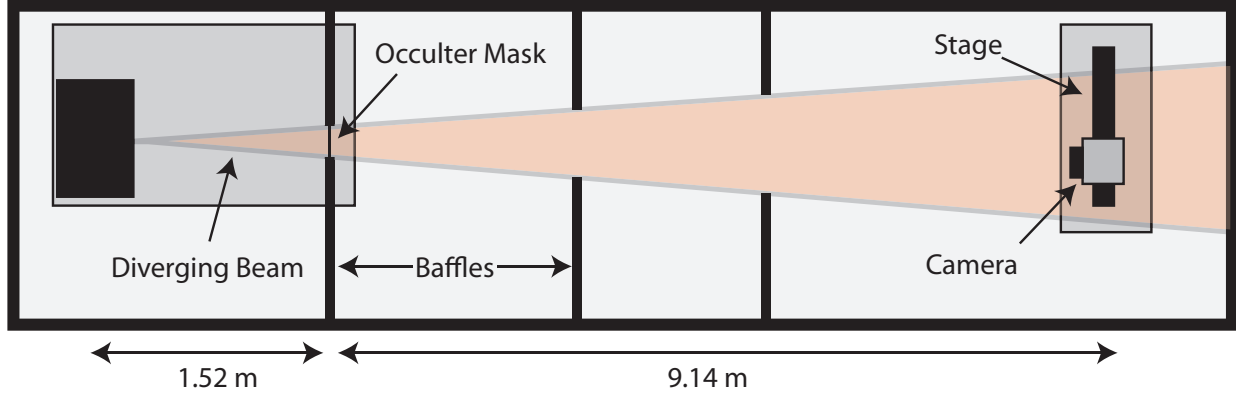


Figure 3: Layout of the Princeton Occulter Testbed. On the left-end of the enclosure is the optical table containing the artificial star and on the right-end is the moveable telescope.

3. EXPERIMENTAL RESULTS

Experimental data is collected by stacking a series of images with identical exposures taken when the camera is aligned with the centre of the shadow cast by the optical mask. The exposure time is chosen to maintain the camera's pixels in their linear regime. To reduce dark noise and camera bias from the stacked frame, for every set of frames collected a set of darks is taken with the same amount of camera exposure but with the artificial star turned off. These dark sets are median-combined and subtracted from each measurement frame to eliminate signals from unwanted sources, such as dark current.

Actual combined image-plane results from a stack of 10,000 frames at 1 sec exposure are shown in Figure 4. To calibrate for contrast, the flux in each pixel of the stacked frame is divided by the peak pixel flux when the mask is removed. To prevent overexposure in the calibration frames, two OD2.0 filters were placed in series before the pinhole. The two OD2.0 filters have measured transmissions of $1.00 \pm 0.01\%$ and $1.05 \pm 0.02\%$. The stacked calibration dataset consists of 100 frames each taken at 0.01 sec to minimize the effect of power fluctuations in the laser source.

In Figure 4(a) the contrast calibrated image plane measurement of the control mask is shown. The control mask dataset consists of 10,000 frames collected at 0.05 sec exposure. Short exposures were necessary to prevent saturation of the bright features of the image while a large number of frames was used to achieve a longer overall integration time allowing features to be seen in the darkest part of the annular region. In Figure 4(b) the contrast calibrated image plane measurement of the optimized occulter mask is shown.

4. THEORETICAL RESULTS

Here we present the optical equations used for the theoretical simulations. First, we propagate the input electric field past the occulter mask to the plane of the camera. The Fresnel propagation for the N-petalized occulter is given by:

$$E_{\text{bin}}(\rho, \phi) = \frac{2\pi}{i\lambda z} \int_0^R E_{\text{in}}(r) e^{\frac{\pi i}{\lambda z}(r^2 + \rho^2)} J_0\left(\frac{2\pi r \rho}{\lambda z}\right) A(r) r dr + \dots \sum_{k=1}^{\infty} \frac{4\pi \cos(kN\phi)}{i\lambda z} \int_0^R E_{\text{in}}(r) e^{\frac{\pi i}{\lambda z}(r^2 + \rho^2)} J_{kN}\left(\frac{2\pi r \rho}{\lambda z}\right) \frac{\sin(k\pi A(r))}{k\pi} r dr \quad (7)$$

Next, we propagate to the image plane from the pupil plane. We define a circular pupil function $p(x, y)$. The expression for the electric field at the image plane defined by Cartesian coordinates (u, v) , ignoring leading phase terms, becomes:

$$E_{\text{im}}(u, v) = \frac{1}{i\lambda s} \iint_{p(x,y)=1} E_{\text{pup}}(x, y) e^{\frac{-\pi i}{\lambda d}(x^2 + y^2)} e^{\frac{-2\pi i}{\lambda s}(xu + yv)} dx dy \quad (8)$$

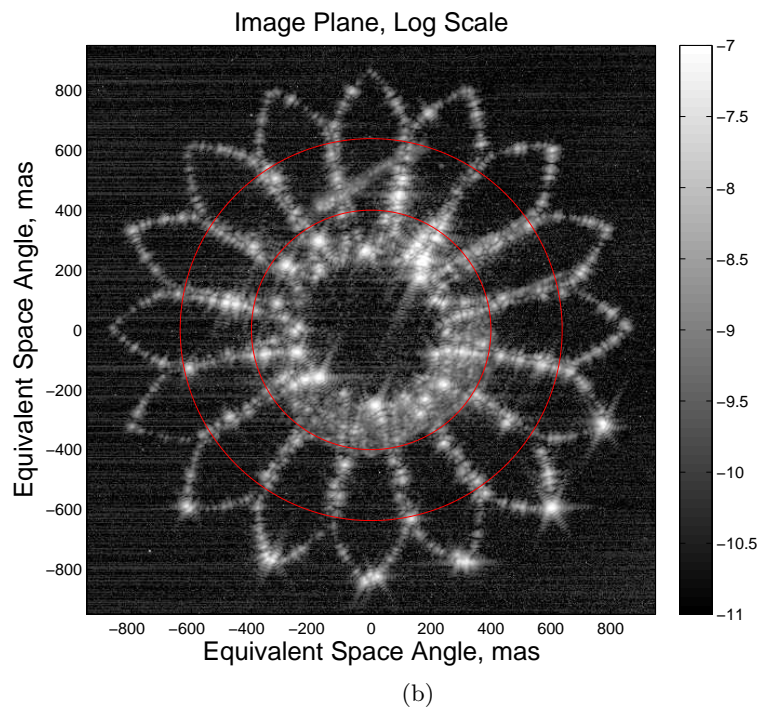
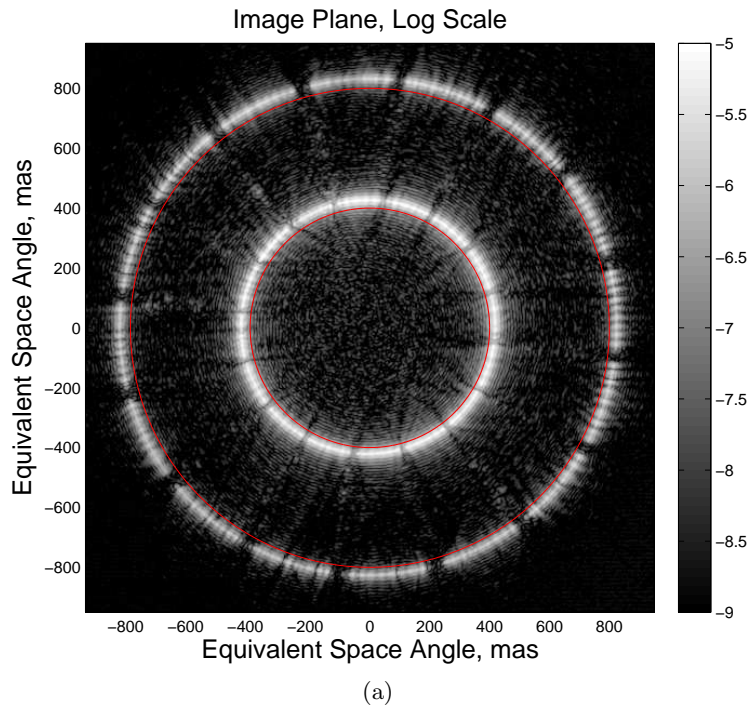


Figure 4: Contrast measurements at the image plane taken (a) using the control mask and (b) using the occulter mask. The inner and outer red circles denote the annular dark region.

We match the experimental setup by selecting the same pixel pitch of the science camera, a radial extent that matches the f-stop, and by choice of the propagation distance s and focal distance d . The image plane simulations for the control and occulter mask are shown in Figures 5(a) and (b) respectively. For the control mask in Figure

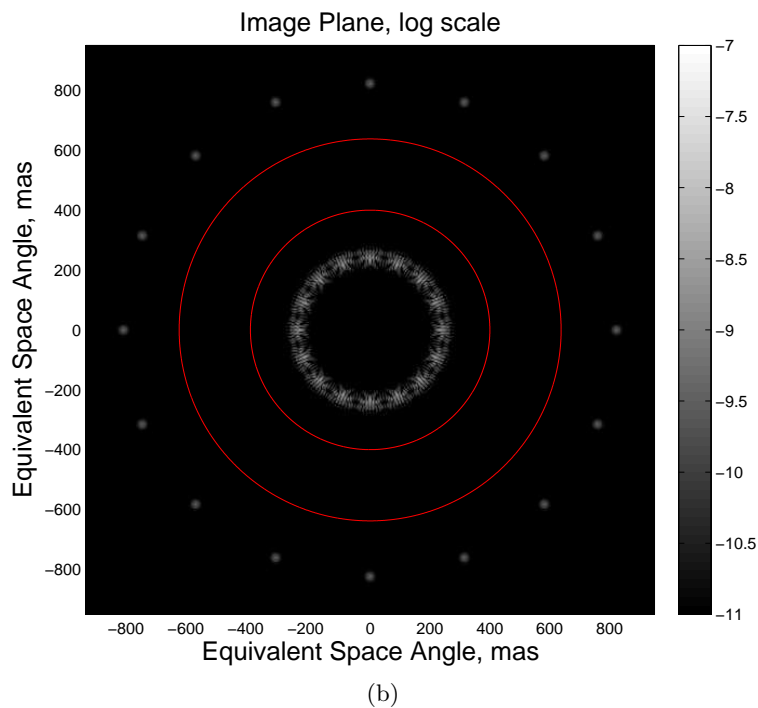
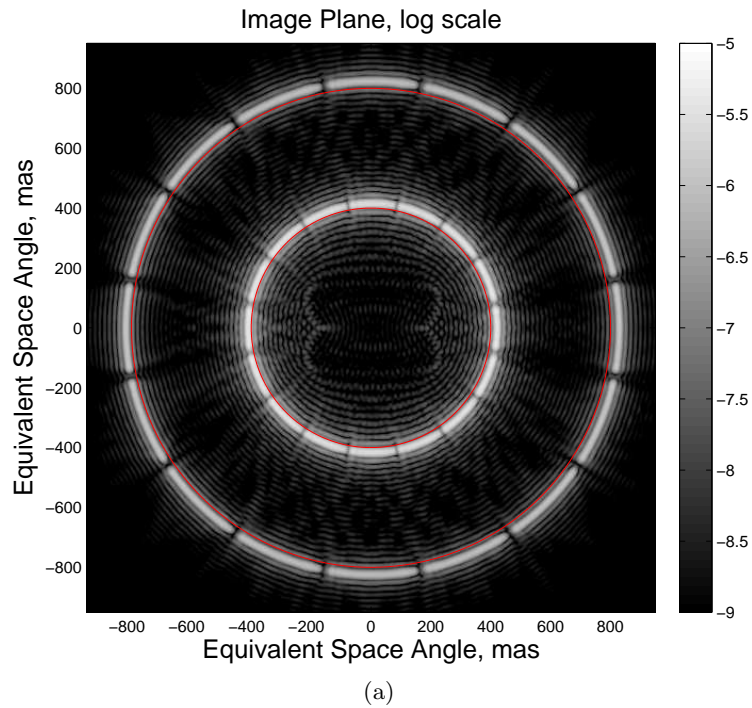


Figure 5: Simulation of contrast in the image plane (a) using the control mask (b) using the occulter mask. The inner and outer red circles denote the annular dark region.

5(a), a 2 mm horizontal displacement is introduced in the camera's location as this eliminated the symmetry of diffraction features (in particular a bright spot at the centre of the image plane) not seen in the measurements.

5. DISCUSSION

We compare the contrast-calibrated image-plane measurement in Figure 4(a) with the theoretical in Figure 5(a). The scalar diffraction simulation captures all the main features of the experimental image: two bright inner and outer rings with sixteen divisions at the point of attachment of the support struts, and fine diffraction ringing around the main bright rings. For a quantitative analysis, we provide a cross-section through the image plane and plot the azimuthal median as shown in Figure 6(a). We also plot a 95 % confidence interval for the median based on percentile populations.¹² The measured inner and outer peaks are both within 50 % of the theoretical. This relatively close agreement demonstrates the validity of the calibration method and scalar diffraction simulation.

However, comparing the occulter mask measurement in Figure 4(b) with the theoretical in Figure 5(b) shows some significant differences. The edges of the measured mask are glinting, much brighter than predicted by theory. The azimuthal median shown in 6(b) shows an improvement of contrast performance over the control mask of about two orders of magnitude. The median contrast across the wedges at the inner working angle of 400 mas space-equivalent is 1.05×10^{-10} and this improves towards the outer working angle at 638 mas space-equivalent to 2.51×10^{-11} . Nonetheless, even inside the dark annular region the optimized occulter mask performs worse than the theoretical diffraction analysis by about two to three orders of magnitude.

To determine the nature of the bright edges on the occulter mask, saturated images of 1800 sec exposure were taken in Figure 7. Figure 7(a) shows the image corresponding to the built-in f/22 iris aperture of the lens, whereas Figure 7(b) is taken with a circular f/22 custom-built aperture. Lastly, Figure 7(c) is taken with a smaller f/47 circular aperture. This set of images is particularly helpful in identifying the glowing edges as glint scattering off the mask's sidewalls. Because the shape of the diffraction spikes changes between Figure 7(a) and 7(b) as the shape of the entrance aperture changes, we may conclude that this is a re-radiated source of light outside of the camera. Furthermore, comparing Figure 7(b) as we decrease the size of the entrance aperture while keeping the same shape, we see that the diffraction rings around the central bright spots increase. Most importantly, these appear to extend into the dark annular regions where they superpose. Figure 8 quantitatively shows the limiting effect of the glint on the contrast performance of the occulter by comparing two different aperture sizes; for the smaller aperture the contrast in the dark annular regions deteriorates as the diffraction rings expand with aperture size. Therefore, we conclude that the glowing edges which are brighter than predicted from the diffraction theory are the limiting factor in verifying contrast in the dark annular regions.

A possible mechanism for the measured bridge edges could be surface plasmonic reradiation due to evanescent coupling resonance – however, we are measuring more than two orders of magnitude enhanced transmission beyond transmission enhancement reported elsewhere due to this effect.¹³ As an additional test, we have placed a narrowband 1 nm filter centred on the laser wavelength on the camera end and the intensity of the glowing edges is comparable to that measured when the same filter is placed before the mask. This indicates that the measured diffraction pattern is not significantly wavelength-shifted, and confirms that it is likely specular reflection rather than plasmonic reradiation.

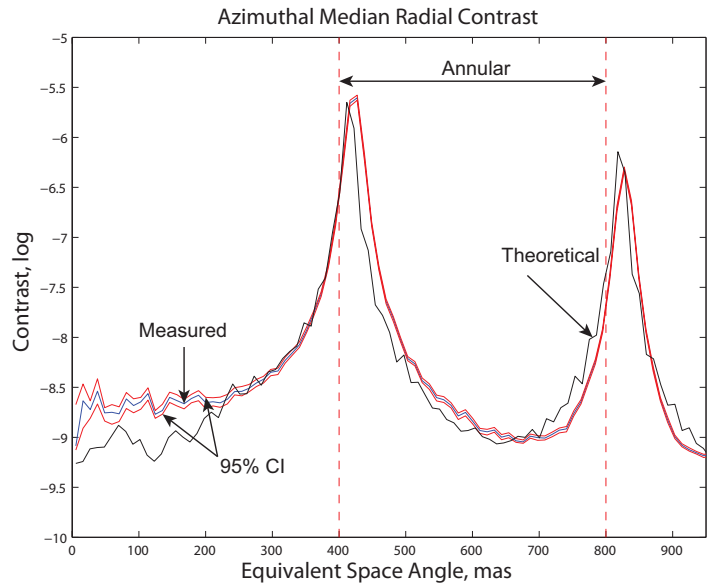
6. CONCLUSIONS

In this paper, we have verified contrast to a level better than 10^{-10} . Using a circular occulter acting as a baseline we have demonstrated that the optimized edge of the occulter improves contrast; the agreement between theory and measurement of the circular mask shows that the contrast calibration method is valid. We are, however, short of the predicted theoretical performance of the occulter mask. This limited performance in the annular dark regions can be attributed due to the extended point-spread function of scattering off the edges of the occulter mask.

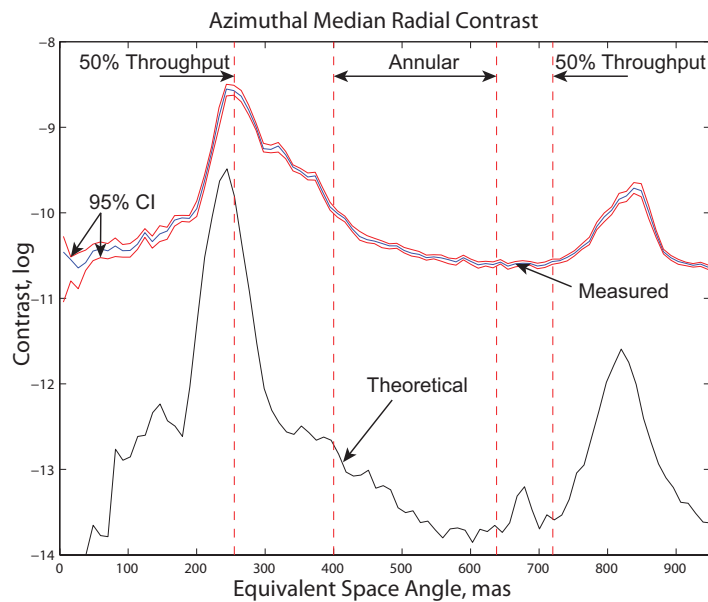
To improve performance for future experiments, we plan to fabricate an identical mask with a process that will reduce the sidewall thickness from 50 μm to approximately 1 μm . Furthermore, the current setup can be used in its current form using a new mask to demonstrate alignment out-of-band leakage – since the contrast will be naturally reduced, the edge scattering should not be a limiting factor and the optical propagation models will be able to predict the diffraction to similar accuracy to the circular control mask.

ACKNOWLEDGMENTS

This work was partially performed under NASA contract NNX09AB97G and a grant 1430187 from the California Institute of Technology's Jet Propulsion Laboratory. DS acknowledges financial support from the the NASA Earth & Space Science Fellowship.

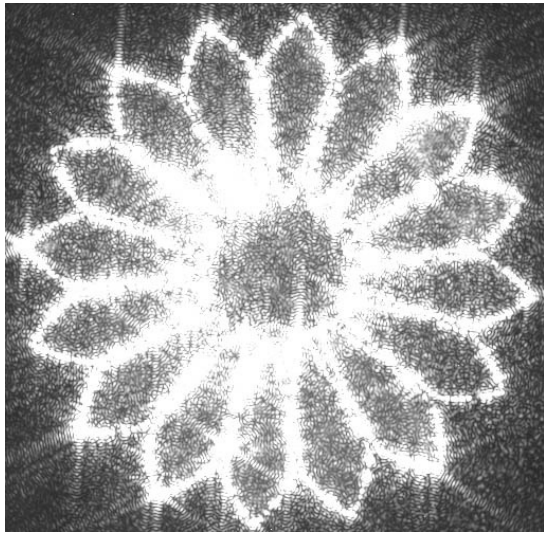


(a)

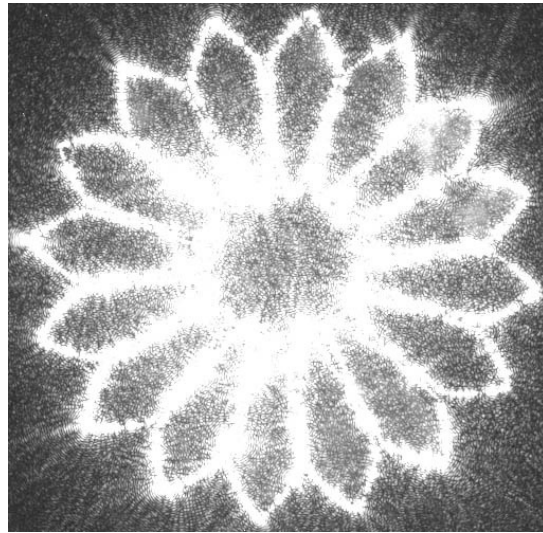


(b)

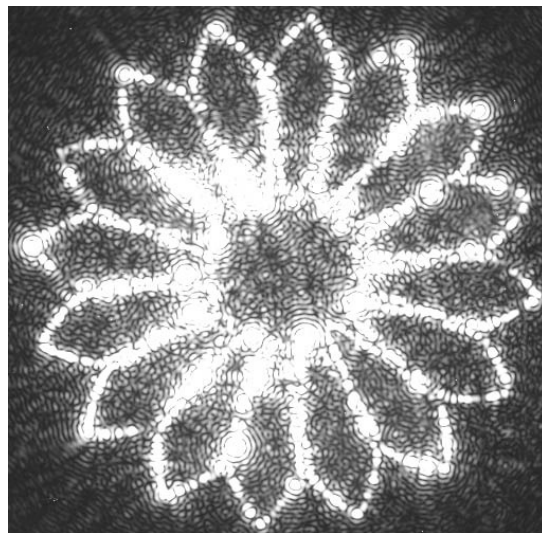
Figure 6: Azimuthal cross-sections through the image plane of (a) the control mask (b) occulter mask comparing the theoretical median with the measured median and its 95 % confidence interval. The dotted vertical lines represent the inner and outer working angles of the annular openings and the 50 % throughput point for the occulter mask.



(a)



(b)



(c)

Figure 7: Equal log-stretched saturated images with different entrance apertures: (a) f/22 iris (b) f/22 circular (c) f/47 circular.

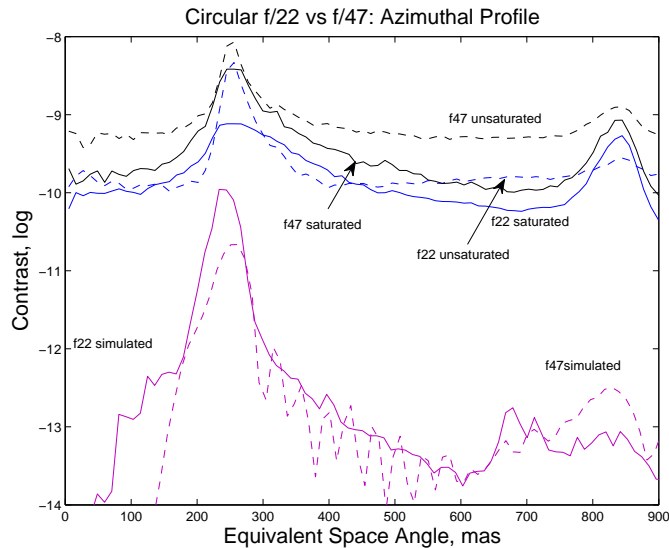


Figure 8: Azimuthal median across the image plane for two circular apertures at $f/22$ and $f/47$. Data was taken for each aperture by stacking both saturated and unsaturated images to accurately capture the valleys and peaks respectively. The theoretical azimuthal plots are offset by 2 mm horizontally from perfect alignment.

REFERENCES

1. D. Des Marais, M. Harwit, K. Jucks, J. Kasting, D. Lin, J. Kunine, J. Schneider, S. Seager, W. Traub, and N. Woolf, "Remote sensing of planetary properties and biosignatures on extrasolar terrestrial planets," *Astrobiology* **2**, pp. 153–181, 2002.
2. L. Spitzer, "The beginnings and future of space astronomy.," *American Scientist*, **50**, 1962.
3. N. J. Kasdin *et al.*, "A telescope for habitable exoplanets and interstellar/intergalactic astronomy," *White Paper*, 2009.
4. W. Cash *et al.*, "New worlds observer," *White Paper*, 2010.
5. N. J. Kasdin *et al.*, "O3: The occulting ozone observatory," *Bulleting of the American Astronomical Society*, 2010.
6. W. Cash *et al.*, "New worlds probe," *White Paper*.
7. N. J. Kasdin *et al.*, "Recent progress on external occulter technology for imaging exosolar planets," *IEEE Aerospace Conference*, 2013.
8. J. Goodman, *Introduction to Fourier Optics*, Roberts & Co., 2005.
9. E. Cady *et al.*, "Performance of hybrid occulters using apodized pupil lyot coronagraphy," *Proceedings of SPIE* **7010**, 2008.
10. R. Vanderbei, D. Spergel, and N. Kasdin., "Circularly symmetric apodization via star-shaped masks.," *Astrophysical Journal* **599**, pp. 686–694, 2003.
11. E. Cady, K. Balasubramanian, M. Carr, M. Dickie, P. Echternach, T. Groff, N. Kasdin, C. Laftchiev, M. McElwain, D. Sirbu, R. Vanderbei, and V. White, "Progress on the occulter experiment at princeton," *Proc. of SPIE*, 2009.
12. R. Hogg and E. Tanis, *Probability and Statistical Inference*, New York: MacMillan Publishing Company, 1993.
13. A. Krishnan *et al.*, "Evanescently coupled resonance in surface plasmon enhanced transmission," *Optical Communications* **200**, 2001.